SAND2022-10878J

Octane Requirements of Lean Mixed-Mode Combustion in a Direct-Injection Spark-Ignition Engine

Namho Kim*, David Vuilleumier, Eshan Singh and Magnus Sjöberg

Combustion Research Facility, Sandia National Laboratories, Livermore, California, USA, 94551.

*Corresponding Author: nkim@sandia.gov

Abstract

This study investigates the octane requirements of a hybrid flame-propagation and controlled-autoignition mode referred to as Mixed-Mode Combustion (MMC), which allows strong control over combustion parameters via a spark-initiated deflagration phase. Due to the throughput limitations associated with both experiments and 3-D computational fluid dynamics calculations, a hybrid 0-D and 1-D modeling methodology was developed, supported by experimental validation data. This modeling approach relied on 1-D, two-zone engine simulations to predict bulk in-cylinder thermodynamic conditions over a range of engine speeds, compression ratios, intake pressures, trapped residual levels, fueling rates, and spark timings. Those predictions were then transferred to a 0-D chemical-kinetic model which was used to evaluate the autoignition behavior of fuels when subjected to temperature-pressure trajectories of interest. Finally, the predicted autoignition phasings were screened relative to the progress of the modeled deflagration-based combustion in order to determine if an operating condition was feasible or infeasible due to knock or stability limits.

Sandia National Laboratories is a multimission laboratory managed and operated by National Technology & Engineering Solutions of Sandia, LLC, a wholly owned subsidiary of Honeywell International Inc., for the U.S. Department of Energy's National Nuclear Security Administration under contract DE-NA0003525.

The combined modeling and experimental results reveal that MMC has an octane requirement similar to modern stoichiometric spark-ignition engines in that fuels with high Research Octane Number (RON) and high Octane Sensitivity (S) enable higher loads. Experimental trends with varying RON and S were well predicted by the model for 1000 and 1400 rpm, confirming its utility in identifying the compatibility of a fuel's autoignition behavior with an engine configuration and operating strategy. However, the model was not effective in predicting (nor designed to predict) operability limits due to cycle-to-cycle variations, which experimentally inhibited operation of some fuels at 2000 rpm. Putting the operable limits and efficiency from MMC in the context of a state-of-the-art engine, the MMC showed superior efficiencies over the range investigated, demonstrating the potential to further improve fuel economy.

Keywords

fuel-lean combustion, mixed-mode combustion, octane requirements, multimode SI engine operation

Introduction

The implementation of a lean-burn advanced gasoline combustion strategy in a commercially available automotive engine has eluded the automotive industry, despite the considerable investments and significant research and development effort in this area over the past three decades. The motivation for lean-burn engines is straightforward – lean combustion systems can offer significant efficiency benefits over stoichiometric operation due to an improved specific heat ratio of the working fluid, as well as lower heat-transfer losses to combustion chamber walls, and in some conditions, a reduction of pumping work. These benefits are particularly significant at low-load conditions, where most stoichiometric gasoline engines operate at only a fraction of their peak efficiency. Despite this, practical implementation of lean combustion engines has been hindered due to challenges with the control of the combustion process, the load range of lean-burn combustion systems, and the cost and challenges associated with lean aftertreatment systems [1]. A wide range of lean-burn advanced combustion compression-ignition approaches using gasoline-range fuels have been investigated [2], ranging from a fully-homogeneous, kinetically controlled approach known as homogeneous charge compression ignition (HCCI) to a heavily fuel-stratified approach known as partially premixed compression ignition. The reactivity controlled compression ignition concept enables to achieve high thermal efficiency (~60%) as well as low engine-out emissions [3, 4]. Additionally, approaches without compression ignition have also been investigated, ranging from fully-stratified-charge spark-ignition operation [5, 6] to homogeneous lean-burn spark-ignition or pre-chamber ignition operation [7]. The aforementioned combustion processes all vary from the traditional stoichiometric-charge spark-ignition process which has been used in gasoline engines for more than a century, by relying either on lean flame propagation or controlled autoignition to achieve lean combustion.

The combustion process which is the focus of the current investigation is a hybrid combustion system relying on both lean flame propagation and controlled end-gas autoignition, here termed as Mixed-Mode Combustion (MMC) [8, 9]. Fundamental autoignition characteristics of MMC were investigated by systematically varying intake oxygen fraction, equivalence ratio, and intake temperature and pressures, as presented in [9]. The MMC system relies on deflagration to consume 50 – 80% of the charge, while relying on controlled autoignition to consume the remainder. The difference in the relative balance between deflagration and autoignition practically alters the engine design requirements, with lower compression ratio (CR) needed to achieve autoignition. This better aligns with a multimode operation strategy where high load operation is enabled by shifting combustion mode from MMC to boosted stoichiometric spark-ignition enables high load operation. The lower CR requirement of MMC allows flexibility to help reduce knocking propensity under stoichiometric conditions at such high loads for a given fuel.

MMC offers advantages relative to other advanced combustion strategies. Keeping combustion duration (CA10 to CA90) short is critical to maximize the benefit of lean-burn combustion, preferably less than 30°CA as indicated in Ref. [10]. Compared to homogeneous lean flame propagation combustion, MMC helps achieve shorter combustion duration, due to the end-gas autoignition event rapidly terminating the combustion event. This helps retain high combustion efficiency and the benefits from lean combustion. In comparison with HCCI operation, MMC affords greater control over the combustion process via the spark phasing, which enables better control authority over the start of deflagration. Conversely, the MMC system offers challenges as well. These include the reliable initiation of the deflagration process in lean mixtures, which is an active area of research. Some emissions formation penalty may be incurred depending on the methodology used (prechamber, advanced ignition system, or stratified charge). In addition, this combustion mode requires reliable cycle-by-cycle control of the end-gas autoignition, which occurs when the fuel, initial condition, boundary condition, and residence time are just right. Weighing the benefits against the challenges listed above, interest has been expressed in putting such a combustion system into production, coupled with stoichiometric operation at high-load conditions [11].

A previous publication showed that for MMC, fuels with similar octane rating, but different octane sensitivities and composition, may show different responses to parametric variation in intake air temperature, pressure, dilution level, and equivalence ratios [9]. However, a thorough investigation on octane-appetite and resultant load limits has not previously been completed for this combustion mode. Such an investigation is needed if the MMC system is to exist in conjunction with a conventional stoichiometric mode for high-load operation.

Modern downsized spark-ignition engines operate at boosted stoichiometric conditions to achieve high load. It was found that fuels with high RON (Research Octane Number) and high S (Octane Sensitivity: defined as a difference between RON and MON (Motor Octane Number)) are beneficial for mitigating knock in downsized spark-ignition engines [12]. If the fuel octane requirements of stoichiometric SI and MMC are very different, it becomes less feasible to implement the two combustion modes in a multimode engine. Therefore, the current study investigated what octane ratings offered the greatest range of operation for the MMC system.

Upon embarking on this investigation, various methods were evaluated for their suitability to assess the octane requirements of MMC. It was determined that to properly achieve this task, a variety of RON and S, covering a practical range of RON (80 – 100) and S (0 – 10) should be evaluated over a wide range of engine operating conditions and configurations (*i.e*. geometric CRs, engine speeds, equivalence ratios, spark timings, trapped residual levels, and intake pressures) for operability and performance. With reasonable parametric sweeps of these parameters yielding tens of thousands of permutations, various methods to evaluate this number of conditions were considered. Experiments have the advantage of capturing all key physics associated with the problem, but a practical throughput of around forty operating conditions per day was deemed insufficient for the number of considered cases. Similarly, an option to utilize computational fluid dynamics simulations was considered given the success in modeling MMC in previous studies [13, 14]. However, the practical throughput of the detailed simulations, even with the use of reduced chemical mechanism, was deemed insufficient to cover tens of thousands of cases. Lastly, 1-D engine simulations with 0-D combustion modeling were considered. Although 1-D simulation tools have the adequate throughput to address the problem scale, existing 0-D or quasi-dimensional combustion models (Ref. [15-17]) were not found to have an appropriate balance of throughput and fidelity for prediction of fuel effects on end-gas autoignition under lean conditions, which is critical for MMC. Therefore it was decided to create a dedicated 0-D combustion model relying on a 0-D chemical-kinetics framework. To model the system with an appropriate level of fidelity and throughput, boundary conditions from 1-D simulations were incorporated into the 0-D chemical kinetic simulations.

To investigate octane requirement that maximizes the MMC operable range, the above mentioned hybrid 0-D and 1-D modeling methodology was utilized to characterize the autoignition tendency of 22 fuels with varying RON and S under thousands of operating conditions. Then the operability of given conditions was determined based on a notional model which was devised using the autoignition phasing and the mass fraction at the autoignition phasing measured experimentally under various engine operating conditions. Lastly, the maximum and minimum loads were found among the operable conditions and the impact of RON and S on achievable loads was studied.

Experimental Setup

The experimental portion of this study was conducted in a spray-guided direct-injection spark-ignition (DISI) single-cylinder research engine. General specifications of the engine are provided in Table 1. Figure 1 (a) shows the cross section of the top-end of the engine, while

Figure 1 (b) shows the cross section of the 3D-CAD rendering of combustion chamber with the piston at 35 degrees crank-angle (°CA) before top-dead center (TDC). In the subsequent sections, crank-angle degrees will be referenced relative to compression TDC.

Throughout the experiments, one of the two intake valves was deactivated to promote strong swirl and tumble flow in the combustion chamber. The in-cylinder flow field for one-valve operation in this engine has been well characterized experimentally and documented in [18]. Under knock-limited conditions for stoichiometric operations, the effect of intake-valve deactivation was found to be minimal at an engine speed of 1400 rpm, causing a change in knock-limited combustion phasing (KL-CA50) of less than 1°CA. The cam shaft phasings that provide both high volumetric efficiency and low residual levels (approximately 3 - 5% by mass) were chosen for the conditions tested in this work.

The engine has a centrally mounted injector closely spaced to a long-reach spark plug. The injector used for the experiments has 8-holes with stepped-hole valve covered orifice. The injector was clocked such that two of the plumes straddle the spark-plug gap as shown in Fig. 1(b). The configuration of the injector and spark plug enables fully stratified-charge operation as well as partial fuel stratification (PFS) where a very small quantity of fuel is injected to initiate more stable and faster deflagration under globally dilute and fuel-lean operation [19].

Table 1: General experimental engine specifications.

Displacement	552 cc
Bore / Stroke	86 mm / 95.1 mm
Connecting rod length	166.7 mm
Geometric CR	12:1
Swirl / tumble indexes (one intake valve deactivated)	2.7 / 0.6
Intake valve diameter	35.1 mm
Intake valve angle relative to cylinder axis	18°
Exhaust valve diameter	30.1 mm

Exhaust valve angle relative to cylinder axis	16°
Fuel injector	Bosch 8-hole HDEV 1.2
Fuel injector hole orientation	Symmetric with 60° included angle
Fuel injector hole size	Stepped-hole, min. diameter = 0.125 mm
Intake valve opening / closing	-359 / -138 °CA (@0.1 mm valve lift)
Exhaust valve opening / closing	149 / -352 °CA (@0.1 mm valve lift)

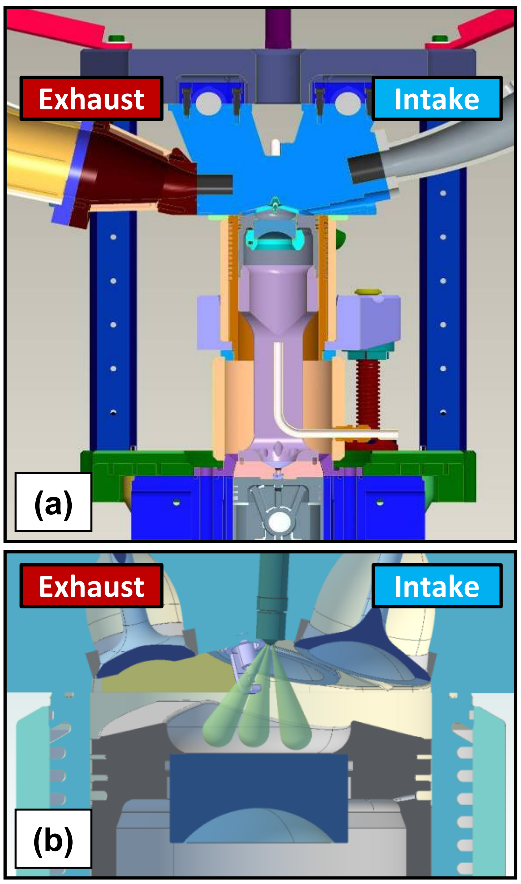

Figure 1 Cross-sections of 3-D CAD rendering of the single-cylinder research engine. (a) Overview of the test engine and (b) combustion chamber geometry at -35°CA.

For each operating point, a sufficient amount of time was spent to stabilize all measured parameters before recording data. During the data acquisition, fuel-flow rate and temperatures from thermocouple readouts were averaged over one minute. The in-cylinder pressure, spark current, intake and exhaust pressure, and fuel rail pressure were acquired using 0.1°CA resolution for 500 consecutive cycles. In-cylinder pressure was measured using an uncooled Kistler 6125C piezoelectric sensor in combination with a Kistler 5010B charge amplifier. The in-cylinder pressure was pegged using the average intake tank pressure at -180 ± 5°CA, which is well before the intake valve closes.

A Horiba MEXA-584L emission analyzer measured carbon monoxide (CO), carbon dioxide (CO_2) and unburned hydrocarbon (UHC). Oxygen (O_2) was measured with a CAI 600PP gas analyzer. Nitric Oxide (NO) and nitrogen dioxide (NO_2) were measured with a CAI 600CLD gas analyzer. Although not reported in the current work, exhaust soot was measured with an AVL 415S smoke meter. Extra air was supplied to the exhaust gas flow at the entry point of the exhaust surge tank. This was done to limit the exhaust gas temperature in the exhaust tank and to lower the dew point of the exhaust gases to avoid loss of UHC and water due to condensation in the unheated exhaust sample lines. With a precisely known exhaust dilution ratio, the measured exhaust composition was back-calculated to engine-out mole fractions.

The apparent heat-release rate (AHRR) was computed from the in-cylinder pressure for each individual cycle using a constant ratio of specific heats (γ) following [20]. The value of γ was chosen to yield a net-zero AHRR during the expansion stroke (i.e. after 60 °CA) well beyond the assumed end of combustion. For stoichiometric operation, typically γ of 1.33 was used. However, for MMC, γ was set to 1.35 to reflect higher γ value of a fuel-lean mixture. For computing combustion-phasing metrics like the 50% burn point (CA50), the AHRR was integrated over the crank-angle range for which AHRR is positive, after the spark discharge. Autoignition phasing and autoigniting mass fraction from experimental data were determined from AHRR. An example for determination of autoignition phasing and autoigniting mass fraction is shown in Fig. 2. Autoignition phasing was defined as the crank angle at which AHRR reaches its local minimum preceding the high AHRR peak dominated by end-gas autoignition.

Autoigniting mass fraction can be obtained by first finding the local-minimum point in the AHRR plotted against the mass fraction burned (MFB). Then the MFB can be subtracted from 1 (i.e. 1-MFB at local minimum AHRR).

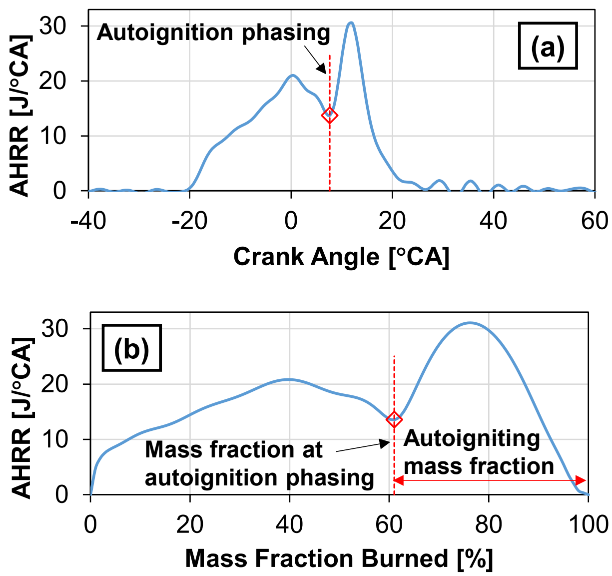

Figure 2. AHRR plotted against (a) crank angle and (b) mass fraction burned. The local minimum AHRR preceding the peak AHRR near the end of combustion is highlighted to indicate crank angle and mass fraction burned when end-gas autoignition dominates combustion.

The Knock Intensity (KI) metric used in this work was calculated from measured cylinder pressure, which was processed on a cycle-by-cycle basis over several steps. First, low frequency content was removed from the measured in-cylinder pressure by subtracting a low-pass filtered (<1.5 kHz) trace from original unfiltered trace. Then the frequency content in the 0 – 80 °CA range was obtained using Fourier decomposition and summed over the frequency range of 5 – 28 kHz. The crank-angle range was limited to increase signal-to-noise of this KI metric. The specific frequency range was chosen to capture the pressure oscillations related to knocking combustion, but to avoid those oscillations related to noise in the sensor or data acquisition system (> 28 kHz) or to the piston motion and deflagration-based combustion (< 5 kHz). Nonetheless, noise in the pressure signal still contributes to the final KI value, and non-knocking cycles result in KI values of 20 – 25 kPa. The reported KI values correspond to the average over 500 cycles. The average CA50 value over the 500 cycles which corresponds to an average KI level of 60 kPa is reported as the KL-CA50. An average KI of 60 kPa results in mild audible knocking with the engine architecture used in this study and the condition is not destructive to the engine even over long timescales. A 60 kPa average KI typically renders a small number of cycles with KI > 400 kPa. Further information on the distribution of KI values of individual cycles for an average KI of 60 kPa may be found in [9].

Experimental Conditions and Procedure

The primary goal of the experiments was to collect a dataset to construct a notional model that determines the operability of given engine operating conditions for various test fuels and find maximum and minimum achievable loads. In addition, the dataset was utilized to validate the model's ability to predict the achievable load range of a fuel at a given engine speed and CR. Therefore, for each tested fuel, the focus of the experiments was on determining load-range limiting cases, such as conditions at which a fuel became too reactive to achieve higher loads, or was not sufficiently reactive to achieve lower loads. The criteria used for defining the load limits were average KI of 60 kPa, and a coefficient of variation (CoV) of gross indicated mean effective pressure ($IMEP_g$) < 3.5%. For each engine operating condition, spark timing (ST) was varied to collect sufficient amount of dataset that satisfies both KI and CoV of $IMEP_g$ criteria.

Two intake pressures (P_{in}), 100 and 130 kPa, were used to test both naturally aspirated and slightly boosted conditions while three engine speeds, 1000, 1400, and 2000 rpm, were used and these cover the majority of the speed range encountered at lighter engine loads for typical powertrain calibrations.

For stable end-gas autoignition for MMC, thermal aid was provided by increasing intake temperature (T_{in}) in 50 – 105°C range using an intake heater installed upstream of an intake surge tank. Intake air was diluted using nitrogen gas (N_2) to reduce intake oxygen mole-fraction (intake [O_2]) down to 15.6 % in order to mimic a practical scenario where charge temperatures are raised by trapping large amount of residual gases using negative valve overlap. Desired flow rates of air and N_2 were achieved using sonic-flow nozzles. When determining fueling rate and air/N_2 flow rate for a given operating condition, charge-mass based equivalence ratio (ϕ_m), as defined in Eq. 1, is utilized as a control variable.

$$\phi_m \equiv \frac{\left(F/C\right)_{Actual}}{\left(F/A\right)_{Stoichiometric}} \quad (1)$$

where F, A, and C are Fuel mass, Air mass, and Charge mass (sum of mass of air and diluent), respectively. ϕ_m is indicative of total chemical energy of the fuel per total amount of supplied gas charge, which is the sum of air and N_2 diluent. Thus, at a given P_{in}, ϕ_m allows the evaluation of how dilute the charge is. When the N_2 dilution level was adjusted, ϕ_m was maintained constant. This results in a change in conventional equivalence ratio (ϕ) which only accounts for the quantity of air and fuel, not inert diluents. The experiments were conducted at three levels of ϕ_m for each P_{in}.

The experiments were conducted using PRF 85 (primary reference fuel with 85% iso-octane and 15% n-heptane by volume), TPRF100S11 (toluene reference fuel with RON = 100, S = 11), and Co-Optima Alkylate (RON = 98, S = 1) to span a wide range of RON and S. Other fuel properties are also given in Table 2. The selected fuels have a limited boiling range and not fully reflective of the distillation characteristics of the market fuels. Nevertheless, the primary focus is given to RON and S in the current study. Fuel properties other than RON and S are considered to have a second order effect based on the previous study (Ref. [9]) that outlined the fuel effects on MMC using a limited number of gasolines that are more reflective of the market fuels. Additional investigations on load limits achievable by fuels that are more representative of market gasolines are beyond the scope of this study and left for future work. The choice of these three fuels will be explained in further detail in the *Model Validation* section.

Fuel was injected using three equally spaced and equally weighted injections starting at -310°CA to realize a well-mixed charge, controlling the end-gas ϕ_m. An injection pressure of 120 bar was used. For stable and fast initiation of deflagration, PFS was utilized by injecting pilot fuel a few crank-angles before the spark discharge. Due to the pilot injection, in-cylinder gases located the central part of combustion chamber are made richer than the end-gas. The ϕ_m reported in the paper refers to that of the end-gas charge as ϕ_m is varied to observe response of end-gas autoignition under various operating conditions. The relative time between pilot injection and spark discharge influences overall combustion stability. Thus, a ST relative to pilot injection that results in the most stable operation was found for each fuel at each operating point. It is desirable to minimize the pilot fuel quantity as much as possible. This is because deflagration in fuel-rich region is known to contribute to elevated formation of thermal NO_x. Thus, the minimum duration of electrical command for the injector was used for pilot injection. As aforementioned in the previous section, advanced ignition systems which could avoid the need for PFS is one active research area. However, concern for the NO_x emissions is out of scope for the current study as the main focus is to determine the octane requirements of MMC.

Experiments for determining the load limits were conducted using the following procedure. For determining upper load limits, operation with ϕ_m = 0.55 and P_{in} = 130 kPa (highest ϕ_m and P_{in}) was first attempted. Given the high P_{in} and ϕ_m, the charge was already reactive enough. Thus, T_{in} = 50°C was used to provide only a minimum thermal aid to stabilize end-gas autoignition at a reasonable range of CA50. If a test fuel was too reactive, P_{in} was reduced to 100 kPa and/or ϕ_m was reduced down to 0.40 in a step of 0.05. Lastly, if the combustion stability for the combination of P_{in} = 100 kPa and lower ϕ_m was unacceptably high, T_{in} was increased as needed. For lower load limits, ϕ_m = 0.35 and P_{in} = 100 kPa was used as a starting point. Low reactivity of the charge was compensated by elevating T_{in} up to 105°C. When T_{in} was increased, additional data were also acquired with more N_2 to reduce intake [O_2] down to 15.6% for mimicking the use of negative valve overlap for increasing reactant temperature. After the high- and low-load limits were determined, the engine speed was altered and the process was repeated, until the limits were determined at all three engine speeds. The parameters varied are shown in Table 3 for reference.

Table 2. Selected fuel properties and ratings for the fuels used for experiment. Those of the Alkylate are adopted from Gage Products and SwRI. The octane ratings of the surrogate fuels were measured using the ASTM D2699 & D2700 methods by SwRI.

	Alkylate	TPRF100S11	PRF85
RON	98.0	100.1	85.0
MON	96.7	89.0	85.0
Octane Sensitivity (S)	1.3	11.1	0.0
AKI	97.3	94.55	85.0
Oxygenates [vol.%]	0.0	0	0.0
Aromatics [vol.%]	0.7	68.7	0.0
Alkanes [vol.%]	98.1	31.3	100.0
Cycloalkanes [vol.%]	0.0	0	0.0
Olefins [vol.%]	0.1	0	0.0
T10 [°C] (most volatile for surrogates)	93	98	98
T50 [°C] (non-surrogates only)	100	-	-
T90 [°C] (least volatile for surrogates)	106	111	99
Net Heat of Combustion [MJ/kg]	44.5	41.6	44.4
Heat of Vaporization [kJ/kg]	309	386	311
AFR Stoichiometric	15.1	13.9	15.1

Average Molecular Formula	C: 7.76 H: 17.45	C: 7.12 H: 10.14	C: 7.84 H: 17.67
Density@15°C [g/ml]	0.6968	0.8128	0.6932

Table 3. Experimental conditions

Engine speed [rpm]	1000, 1400, 2000
Coolant temperature [°C]	75
Intake pressure (P_{in}) [kPa]	100, 130
Injection pressure [bar]	120
SOI_e (electrical start of injection for triple injections) [°CA]	-310, -290, -270
Intake [O_2] [%]	15.5 – 20.9
ϕ_m (charge mass-based equivalence ratio) [-]	0.35 – 0.55
Intake air temperature (T_{in}) [°C]	50 – 105

Modeling Approach

In order to assess the octane appetite of the MMC over a wide range of operating conditions, a hybrid 1-D & 0-D modeling framework was implemented. It should be reiterated that such modeling approach was selected to achieve a good balance between throughput and fidelity of simulation results. Figure 3 provides an overview of the modeling workflow and hierarchy. First, 1-D simulations were conducted in GT-Power [21], spanning the ranges of CR, engine speed, P_{in}, ϕ_m, ST (manifested as changes in CA50), and BDC temperature (T_{BDC}) listed in Table 4. In GT-Power simulations, instead of altering T_{in} like for experiments, T_{BDC} was adjusted to match that from experiments. Next, the results of the 1-D simulations were used to impose initial temperature and pressure boundary conditions on a CHEMKIN 0-D reactor model. The closed homogeneous reactor model, which simulates the autoignition process for a given fuel when subjected to a given pressure history, was run at each operating condition with each of the fuels listed in Table 5. A depiction of the reactor model autoignition calculation is shown in Fig. 3, which overlays the calculated temperature-pressure trajectory onto a non-reacting adiabatic compression trace, with both traces overlaid on constant-volume ignition delay contours. Lastly, the information on autoignition phasing and mass fraction at the autoignition phasing from simulations and viable operating space predetermined from experimental results were utilized to determine the operability of a given operating condition. More details about the framework are presented below.

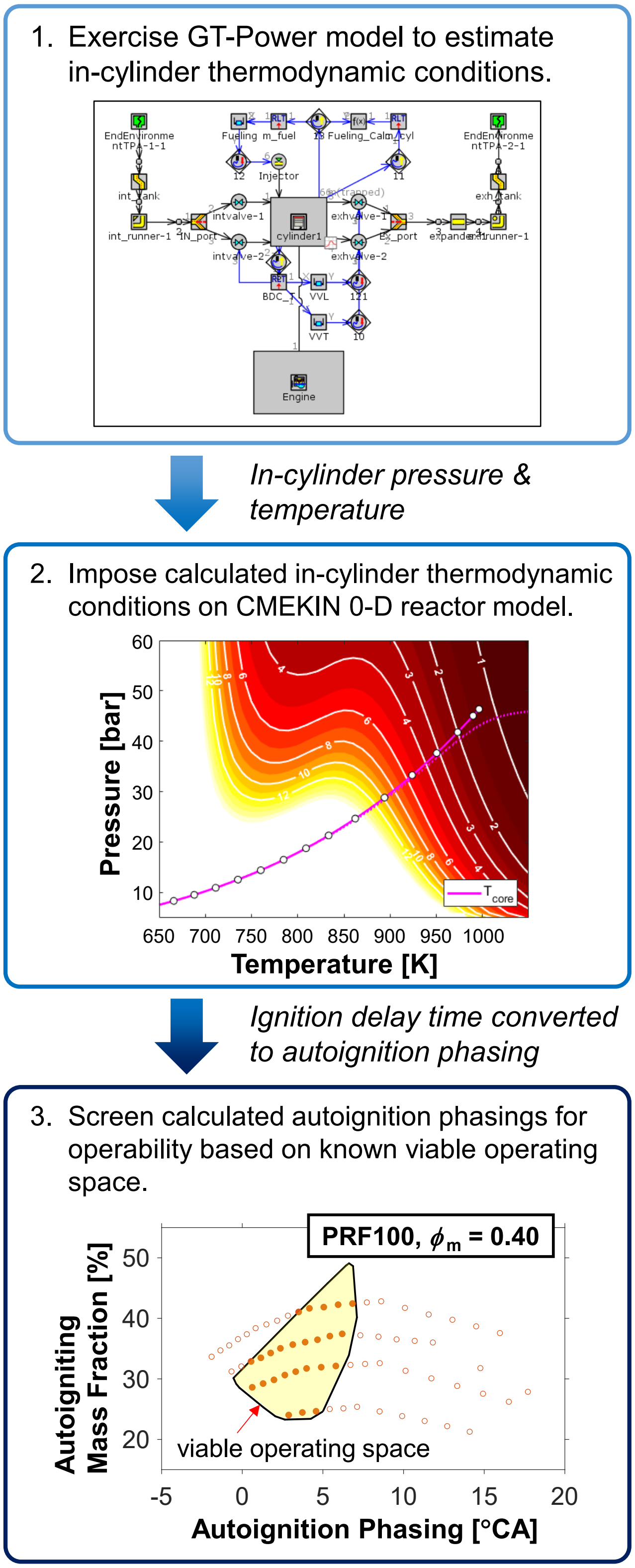

Figure 3: Diagram of the modeling workflow, encompassing the 1-D GT Power model, the 0-D kinetics model, and the screening of operating conditions for feasibility.

Table 4 GT-Power simulation conditions. Each variable was spanned parametrically, resulting in 4320 cases in total.

Geometric CR [-]	12, 13, 14
Engine speed [rpm]	1000, 1400, 2000
Intake pressure (P_{in}) [kPa]	85, 100, 115, 130
ϕ_m [-]	0.35, 0.4, 0.45, 0.5, 0.55
CA50 [°CA]	-10, -5, 0, 5, 10, 15
BDC temperature (T_{BDC}) [°C]	85, 100, 115, 130
Intake air temperature [°C]	25

Table 5: List of fuels evaluated computationally. Composition of the fuels (iso-octane, n-heptane, and toluene) is in mole fraction. The TPRF compositions needed for achieving the target RON and S were obtained using CloudFlame provided by King Abdullah University of Science and Technology (KAUST), Saudi Arabia.

#	Name	RON	S	C_8H_{18}	C_7H_{16}	$C_6H_5CH_3$
1	PRF100	100	0	1.00	0.00	0.00
2	PRF98	98	0	0.98	0.02	0.00
3	PRF95	95	0	0.94	0.06	0.00
4	PRF91	91	0	0.90	0.10	0.00
5	PRF89	89	0	0.88	0.12	0.00
6	PRF87	87	0	0.86	0.14	0.00
7	PRF85	85	0	0.84	0.16	0.00
8	PRF83	83	0	0.81	0.19	0.00
9	PRF81	81	0	0.79	0.21	0.00
10	PRF79	79	0	0.77	0.23	0.00
11	TPRF100S10	100	10	0.21	0.12	0.67
12	TPRF98S10	98	10	0.19	0.14	0.67
13	TPRF95S10	95	10	0.16	0.17	0.67
14	TPRF91S10	91	10	0.13	0.21	0.66
15	TPRF100S7	100	7	0.45	0.08	0.47

16	TPRF98S7	98	7	0.43	0.10	0.47
17	TPRF95S7	95	7	0.40	0.13	0.47
18	TPRF91S7	91	7	0.37	0.17	0.46
19	TPRF89S7	89	7	0.34	0.19	0.46
20	TPRF87S7	87	7	0.32	0.21	0.47
21	TPRF85S7	85	7	0.31	0.23	0.46
22	TPRF83S7	83	7	0.29	0.25	0.46

A GT-Power model of the experimental engine was developed (*cf*. Fig. 4) and validated over a wide range of conditions. For the in-cylinder combustion model, multiple Wiebe functions (Ref. [22]) were utilized for prescribing heat release rate. This approach superposes several Wiebe functions and better mimics the experimentally measured HRR profiles compared to using a single Wiebe function. The coefficients in the multi-Wiebe functions were tuned based on the experimental data. A portion of the model validation is shown in Fig. 5(a), which plots predicted (hollow markers) and observed (solid markers) mass flows into the motored engine over a range of engine speeds and P_{in}s. Figure 5(b) and (c) show that the predicted in-cylinder pressure agrees well with the experimental data for both motored and fired operation. Additional validation results for GT-Power model developed at Sandia can be found in Ref. [23]. The validated GT-Power model was exercised over a wide range of operating conditions, listed in Table 4, to generate in-cylinder thermodynamic conditions which could be passed on to kinetic simulations.

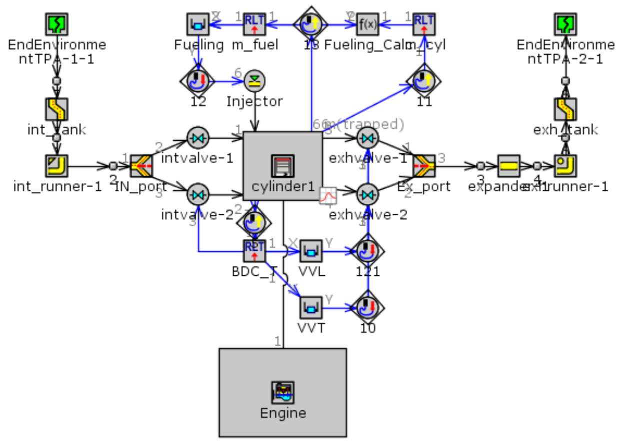

Figure 4: GT-Power model diagram of the single-cylinder engine model used in this study.

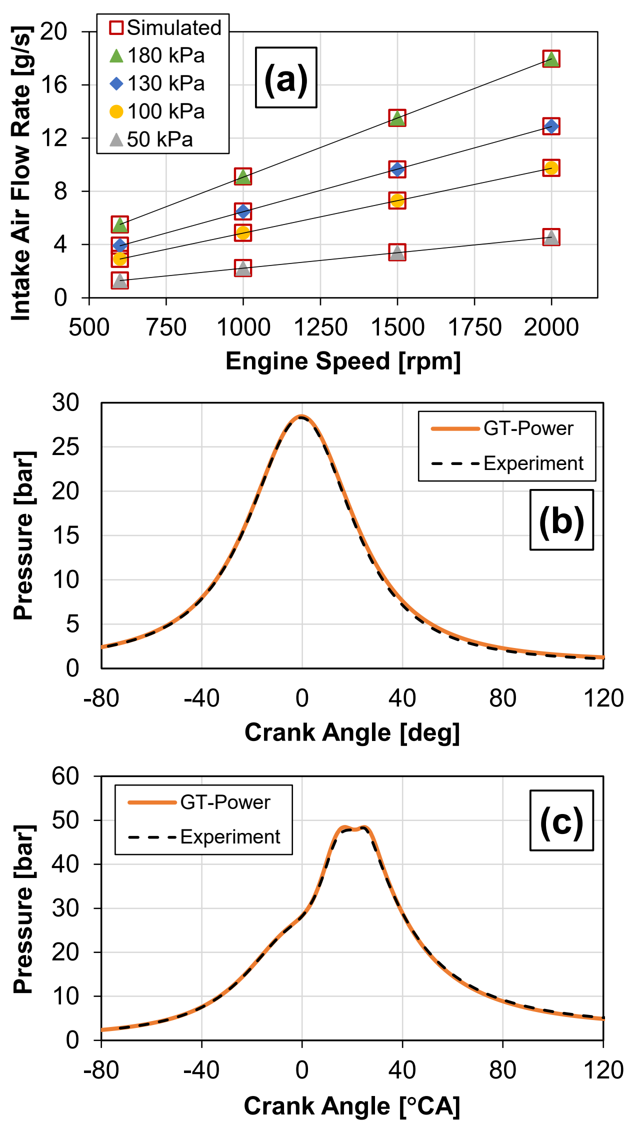

Figure 5: (a) Validation of the GT-Power model against experiments under motored conditions for a range of speeds and intake pressures. Experimental results are shown with solid symbols whereas the simulation results are indicated by hollow red squares. An example of comparing in-cylinder pressure traces under (b) motored and (c) fired operation predicted by GT-Power against experimental data.

After validation of the model against experimental results, variable valve timing and lift were added along with PID controllers for these components. The use of variable valve timing and lift enables an adjustment of the amount of trapped residual to achieve a desired T_{BDC} without altering T_{in}. A greater negative valve overlap, manifested by early exhaust valve closing and late intake valve opening, results in higher T_{BDC} but reduced mass of intake air. In this way, realistic combinations of T_{BDC}s and in-cylinder [O_2] were achieved for each condition, rather than in the experiment, where intake [O_2] was varied independently from T_{in} for simplicity. Figure 6 illustrates in-cylinder [O_2] calculated in GT-Power for given T_{BDC}s. Variations in in-cylinder [O_2] exist because the target T_{BDC} was achieved using variable valve timings and lifts to alter the amount of trapped exhaust gas residuals. Depending on $IMEP_g$, ϕ_m, CA50, P_{in}, and engine speed, the temperature of the residual gas changes which alters the required amount of hot trapped residuals for meeting the target T_{BDC}. Consequently, the in-cylinder [O_2] varies between operating conditions. For the highest T_{BDC}, a larger amount of trapped residual mass is generally needed, especially for lower engine loads, and hence a greater variation in in-cylinder [O_2] is observed. However, the combinations of T_{BDC} and in-cylinder [O_2] are reasonably close to those used in the experiments as demonstrated in Ref. [9].

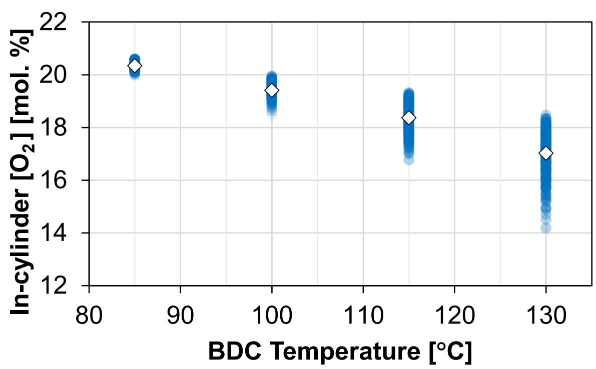

Figure 6: Simulated in-cylinder [O_2] at various T_{BDC}s. The blue markers indicate individual data point whereas the white markers indicate the average values over a wide range spanned in GT-Power simulations.

For chemical-kinetics simulations, a 0-D homogeneous batch reactor model in CHEMKIN was utilized [24]. Previous studies demonstrated that imposing an in-cylinder pressure trace as a time-varying boundary condition enables to sufficiently model the compression of the end-gas by expanding flame and piston motion [25-27]. The same methodology was followed in this study using in-cylinder pressure traces obtained from GT-Power simulations. Initial temperatures used for the 0-D reactor simulations were also provided by GT-Power. A detailed chemical kinetic mechanism developed by Lawrence Livermore National Laboratory (LLNL) was used for chemical-kinetics simulations [28]. This mechanism contains 2871 species with 12804 reaction steps. The LLNL detailed mechanism was selected as it was proven to be reliable when utilized for the modeling approach used in this study. In addition, in a separate study at Sandia National Laboratories, it had been demonstrated that an optimal fuel for low-temperature gasoline combustion (LTGC) could be designed successfully using the LLNL detailed mechanism [29]. Based on the findings in Ref. [9] that NO can play an important role for the autoignition processes under MMC conditions, a fixed NO level of 10 ppm was included in the reactants for all cases. In practice, changes in engine operation and valve strategy can alter the amount of NO. This difference between experiments and modeling adds an uncertainty to the autoignition phasing calculations, estimated as follows. According to Ref. [9], the autoignition phasing changes by less than 2.5 °CA when NO is increased from 0 to 50 ppm. The maximum NO level observed from the experiments is ~46 ppm, which renders the maximum possible offset in autoignition phasing prediction to be less than 2°CA. This level of uncertainty is considered acceptable given the objectives of this study. A refined treatment of NO effects is left for future work where more realistic gasoline-like fuels are sought for maximizing MMC operability. In can be noted that NO sensitivity may differ between fuels, even when RON and S are the same [30]. The output of the reactor model (ignition delay) was defined as the time at which the reactor temperature exceeded a threshold of 1500 K. The ignition delay calculated from the reactor model was converted to autoignition phasing in crank angle degrees relative to compression TDC for the given engine speed. The autoignition phasing was then used to calculate the autoigniting mass fraction based on unburned mass fraction calculated in GT-Power. Figure 7 shows that the autoignition phasing can be predicted within -3 to 0°CA under various operating conditions at 1400 rpm. The error of -3°CA in the autoignition phasing can impact the determination of operable $IMEP_g$ range. However, it was found that -3°CA shift in autoignition phasing corresponds to 2 – 3% change in the predicted $IMEP_g$ limit, which was deemed acceptable for the current validation.

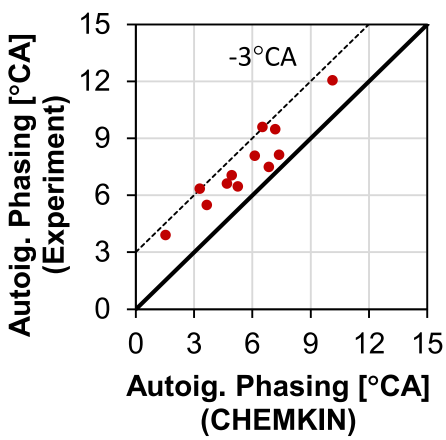

Figure 7. Validation of autoignition phasings under various operating conditions. The dotted line corresponds to CHEMKIN simulation results 3°CA earlier than experimental data.

The concept of the screening method is depicted in Fig. 8. If the autoignition phasing is too early in the cycle, before a sufficient level of charge has been consumed by deflagration, then a large fraction of the charge autoignites which is highly likely to result in strong knock, making the operating condition unviable. Conversely, if the autoignition occurs too late in the cycle, after the majority or all of the charge has been consumed by deflagration, then the combustion duration becomes excessive. This results in intolerable cycle-to-cycle variations in $IMEP_g$, due to the autoignition of some cycles and not others, again limiting operability. Based on these two primary limits, an operational space can be defined, which depends on the amount of charge consumed by autoignition, the autoignition phasing, and the ϕ_m. The operational space was defined using the experimental results of the three test fuels, covering various combinations of P_{in}, T_{in}, intake [O_2], and ϕ_m (*cf.* Table 4). This operational space, defined by the autoigniting mass fraction, autoignition phasing, and ϕ_m, is depicted in Fig. 9. The defined operational space was used to categorize all conditions (engine parameters and fuel combinations) into operational or non-operational categories. Coupled with the 1-D simulation data, which provided $IMEP_g$ of each operating condition, the operational categorization allowed the load range of each fuel to be quantified at each engine speed and CR combination.

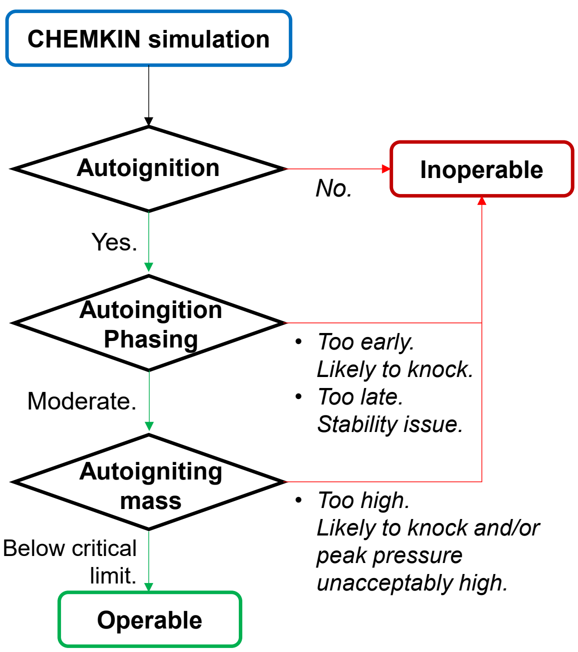

Figure 8. A flow chart to visualize the logic used to determine the operability of a given simulation condition.

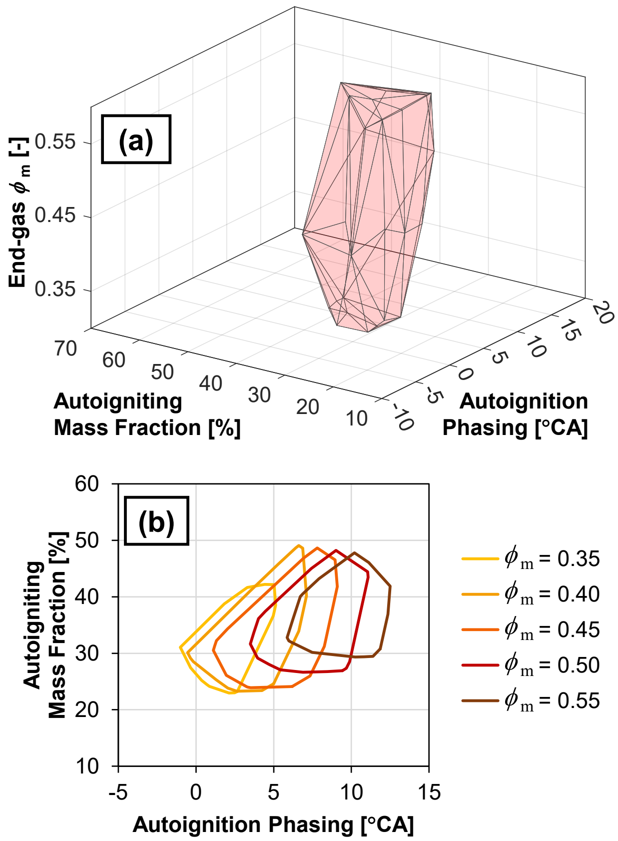

Figure 9. (a) Three-dimensional operational space defined by autoigniting mass fraction, autoignition phasing, and ϕ_m for the MMC system. (b) Two-dimensional slices of the three-dimensional operational space at various ϕ_m.

The described approach was utilized to screen 22 fuels of varying composition, as listed in Table 5, spanning a range of reactivities and autoignition behaviors. The evaluated fuels comprised of ten PRFs ranging from RON = 79 – 100, eight TPRFs with S = 7 and RON = 83 – 100, and four TPRFs with S = 10 and RON = 91 – 100. Although PRFs and TPRFs are not fully representative of the compositions in market gasolines, simple fuel formulations with varying RON and MON are deemed sufficient for the initial assessment of the octane appetite of MMC and load limits. It is also worth reiterating that the model was designed to capture major reactivity effects on operability, such as cases in which a fuel is too reactive to operate effectively at high-load conditions (even with significant ST retard), or too reactive to operate at low engine speed (which affords greater timescales for autoignition), or too unreactive to allow operation with a low CR and a higher engine speed at low loads. The model was not designed to evaluate a fuel's suitability from other standpoints, such as distillation curve (ability to form an ignitable mixture), laminar burning velocity characteristics, knocking tendency at a fixed autoignition level, characteristic cycle-to-cycle variation, or other factors. Particularly, the effects of thermal stratification on end-gas autoignition behavior, as well as the resulting rate of heat release and KI, have been shown to have a measureable effect on operability and ultimate fuel performance, both in the MMC system and in a stoichiometric-dilute combustion system [9, 27]. Despite the aforementioned physics which were omitted by the model's description of the physical system, the treatment of the problem was deemed appropriate for the task of fuel screening in cases where the evaluated fuels were limited to what could fairly be described as simple kinetic surrogates for gasoline.

Finally, the model outputs may be further utilized to construct steady-state engine operating maps which can be utilized in drive-cycle simulations to predict vehicle fuel economy. Figure 10 shows an example where brake efficiency map within the MMC operable range are illustrated. Brake mean effective pressure (BMEP) was obtained in GT-Power by assuming a constant friction mean effective pressure (FMEP) of 0.5 bar. For boosted operations, the exhaust back pressure was assumed to be higher than the intake pressure by 0.05 bar. Such efficiency map could either be coupled with a series hybrid-electric vehicle model to assess the viability as a stand-alone combustion mode, or, perhaps more practically, be combined with an operating map for a second combustion mode, such as a stoichiometric spark-ignition mode, which would be in-line with the multimode operation discussed in the *Introduction*.

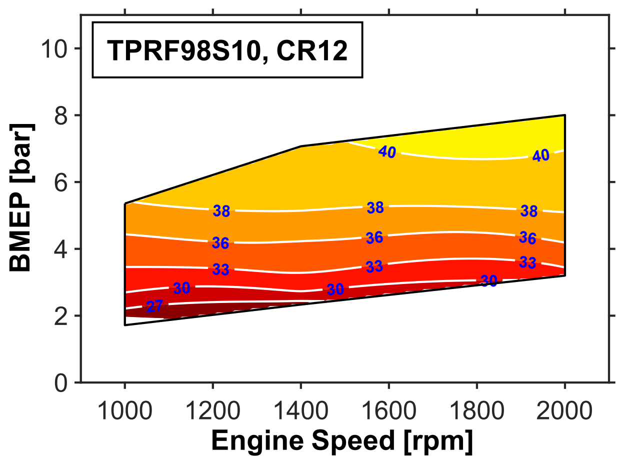

Figure 10. Simulated operating range for MMC operation across the tested speed and load range, with brake efficiency plotted for the TPRF98S10, CR = 12.

Results and Discussions

Model Validation

The 1-D/0-D model framework was validated by comparing the predicted maximum $IMEP_g$ with the measured values for three engine speeds. Figure 11 shows the predicted and measured $IMEP_g$. $IMEP_g$ was compared instead of 'net' indicated mean effective pressure ($IMEP_n$). This is because the breathing of the actual engine was different from the GT-Power model which utilized a negative valve overlap strategy to trap more residual to control T_{BDC} whereas in the experiments, T_{in} was adjusted while keeping the valve timings unchanged. Nevertheless, measured and predicted $IMEP_g$ can still vary because volumetric efficiency is not identical and the resultant fueling rate differs. Thus, a focus should be given to the change in maximum $IMEP_g$ associated with RON and S.

TPRF100S11 exhibits the highest load limit among the three fuels. As the engine speed increases from 1000 to 1400 or 2000 rpm, a significant gain in the maximum $IMEP_g$ is observed.

The model precisely captures both the greater $IMEP_g$ limit for TPRF100S11 and the increase in maximum $IMEP_g$ for higher engine speeds. PRF85 shows a good agreement between the predicted and measured maximum $IMEP_g$ at 1400 rpm. At 1000 rpm, the model predicts that a potential operable space for PRF85 exists even though operable points were not found from the experiments. The observed discrepancy partly arises from the additional P_{in} explored in the simulations in contrast to the limited P_{in}s used in the experiments (*cf*. Table 3 and 4). The model predicts that operable space for MMC exists when P_{in} = 85 kPa is used. If P_{in} = 85 kPa is removed from the screening process, the model indicates that there are no viable operating condition, which agrees with the absence of experimental data point at 1000 rpm. At 2000 rpm, it was found experimentally that even if ST was adjusted, all of the operating conditions resulted in either too knock-limited or too unstable combustion based on the criteria used for screening the viable operating conditions. A more detailed explanation will be shown in the following paragraph. For Alkylate[1], the maximum $IMEP_g$ is reasonably predicted by the model for 1000 – 1400 rpm. However, a discrepancy arises in the case of operation with Alkylate at 2000 rpm. Unlike the experimental results which does not show an increase in the maximum $IMEP_g$ for higher engine speed, the model predicts a significant gain in the maximum $IMEP_g$ as the engine speed is increased to 2000 rpm. At 2000 rpm, it was difficult to acquire experimental data with simultaneously acceptable KI and combustion stability similarly to PRF85. Next, a detailed analysis on the experimental results will show why the operation at 2000 rpm was so limited with the current engine hardware.

[1] Surrogate formulation for Alkylate: n-butane (1.6%), 1,2,4-trimethylbenzene (2.3%), n-pentane (5.5%), and iso-octane (90.6%) in mole fractions.

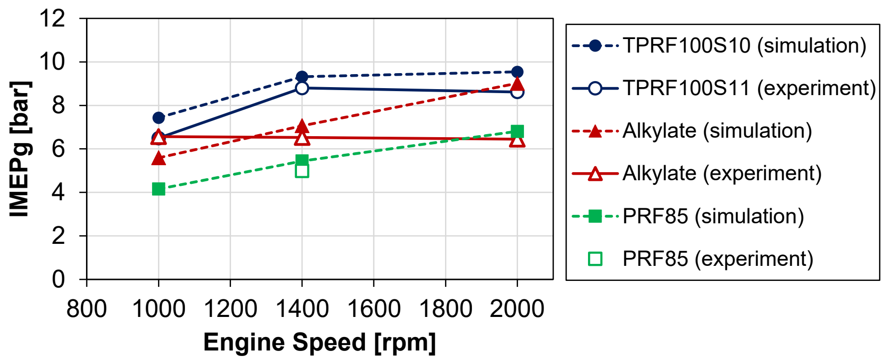

Figure 11. Measured and predicted maximum $IMEP_g$ at three engine speeds for TPRF100S11, Alkylate, and PRF85. Experimental data are shown in open symbols whereas the simulation results are shown in closed symbols.

A detailed analysis of the experimental validation dataset showed that whereas the fuel's operating range at the lower engine speeds is primarily determined by the overall reactivity profile, the primary factor in determining operability at 2000 rpm is the relationship between cycle-to-cycle variations (CCV) in CA50 and knock. The Alkylate and TPRF100S11 fuels both have similar RON levels and in some cases, such as 2000 rpm, ϕ_m = 0.45 and 0.55, similar CA50s are required for achieving end-gas autoignition. In Fig. 12, it may be seen that for similar operating conditions and average CA50, the two fuels exhibit slightly different responses of KI variations to variability in CA50. At the condition shown in Fig. 12, Alkylate and TPRF100S11 have nearly identical levels of CA50 variation (standard deviation (σ) = 2.18 and 2.02, respectively, an 8% difference), but significantly different levels of KI variation (σ = 70 and 47, respectively, a 47% difference), as visualized by the markers indicating average KI and CA50, as well as markers indicating the average values plus or minus one σ. The difference in slope between CA50 and KI is also visible for the two fuels. This seemingly minor difference in slope is important at 2000 rpm, where characteristic σ of CA50 are on the order of 2.1 °CA, compared to 1.4 °CA at 1000 rpm. These three factors – slightly higher CA50 variations at higher engine speed, the higher overall CA50 variations observed for all fuels at 2000 rpm, and a higher knock response for cycles with advanced CA50 – combine to force Alkylate to operate at retarded CA50 to maintain average KI = 60 kPa. However, the operation at late CA50 results in high CoV of $IMEP_g$, which heavily restricts the Alkylate fuel's operation at 2000 rpm. A similar explanation can be applied to the highly limited operability of PRF85 at 2000 rpm. In order for the model to capture these effects, the model would likely need to estimate both an individual fuel's KI response to CA50 advancement, as well as the characteristic increase in CA50 variability at higher engine speeds. Previous research [26, 27] has suggested that the interactions between a fuel and the end-gas's characteristic thermal stratification has a role in determining the relationship between autoignition phasing, peak AHRR associated with autoignition, and knock response.

The dependence of high-speed operation on end-gas heat transfer behavior that affects end-gas thermal stratification and CA50 variability points to the dependence of the results on the engine hardware, and the possibility for optimization of the engine hardware and the combustion system. Additionally, while these observations suggest that specific results will be hardware dependent, it is likely that the overall trends in fuel's reactivity versus operable range are more universal, based on the ability of the model to capture the general behavior of the system at lower engine speeds without information on end-gas thermal stratification or cycle-to-cycle variations. Put differently, the model predictions of the effects of RON and S on the load range should be interpreted as representative of an engine with a combustion system for which cycle-to-cycle variability remains low for all fuels and engine speeds.

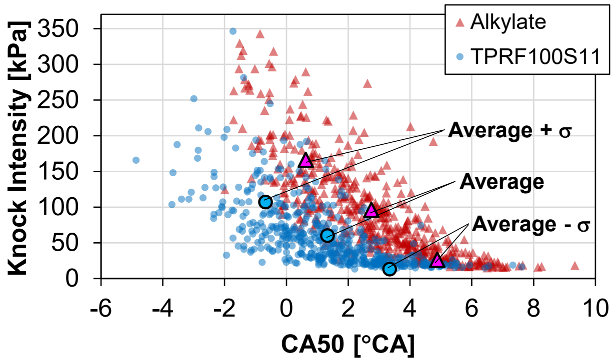

Figure 12. Experimental knock-intensity distributions as a function of CA50 for Alkylate and TPRF100S11 at 2000 rpm, ϕ_m = 0.55.

Influence of RON and S on Operable Range of MMC

The MMC operability model was used to evaluate the operating range of 22 fuels (*cf.* Table 5) at three engine speeds (1000, 1400, and 2000 rpm) and three CRs (12, 13, and 14). The model provided insight into the interaction between a fuel's reactivity and its operation in a MMC system. It is worthwhile to reiterate that the MMC operation is limited by conditions in which the charge is not reactive enough to autoignite, even with very advanced ST, or where the charge is so reactive that the ST must be retarded beyond the stability limit to avoid strong knock. Of course, the reactivity of the charge is dependent on a number of factors, including the operating conditions, engine configuration, and the fuel's reactivity profile.

The modeling results of the current investigations reflect this knowledge which has been accumulated from previous investigations. Figure 13 plots the operating conditions which were tested for two RON100 fuels but different S (0 versus 10) at 1400 rpm and CR = 12. These operating conditions are plotted in terms of autoigniting mass fraction, end-gas autoignition phasing, and ϕ_m, relative to the operability limits which were imposed (depicted as a 3D pink polygon, *cf.* Fig. 9(a)). The autoignition phasing is a function of the ST imposed on the model as well as the fuel's autoignition behavior, as predicted by the chemical kinetic calculations. Similarly, the autoigniting mass is a function of the state of combustion progress at the onset of autoignition, making this also a function of the deflagration and autoignition processes. Each point shown in Fig. 12 is reflective of a particular P_{in}, T_{BDC}, ϕ_m, and ST. Figure 13 indicates how the operability space interacts with the fuel's response to changing operating conditions, allowing operation of certain conditions and not others. The figure also highlights how the shift to higher P_{in}, thereby raising the reactivity of the charge, poses operability challenges for the low-S PRF100 fuel. Figure 13 shows that the low-S fuel has only a few points deemed operable for P_{in} = 130 kPa. Conversely, the high-S fuel maintains a reasonably large number of operable points under the boosted condition

Figure 14 presents the operability of a sequence of fuels, ranging from PRF 79 to PRF 98 for 1400 rpm, CR = 12, P_{in} = 100 kPa in the same format as Fig. 13. Only P_{in} = 100 kPa is shown because at 1400 rpm, CR = 12, most of the PRFs are inoperable at P_{in} = 130 kPa. Figure 14 shows that as the RON of the fuel increases, a larger number of evaluated points fall into the operability space, particularly those with higher ϕ_m. Interestingly, for the most part this does not necessarily accompany loss of operability for conditions with lower ϕ_m (see markers in Fig. 14 for the lower ϕ_m); this behavior was observed experimentally as well. The observed behavior runs counter to the notion that low-RON, high-reactivity fuels may be an optimal fit for this combustion system, due to much stronger performance at low-load conditions which are practically achieved with lower ϕ_m and/or lower P_{in}. Instead, high-RON fuels exhibit minimal penalties at low-load conditions, while realizing significant expansions in operability at high-load conditions. These results are contingent on the choice of investigated conditions, namely the CRs and engine speeds which have been tested. However, these conditions are reflective of the engine speeds which characteristically make up significant portions of federal test procedures [31], and at which other fuel-saving technologies, such as cylinder deactivation, are active [32].

The CRs which were tested are reflective of those found in the market for high-performance and high-efficiency naturally aspirated engines.

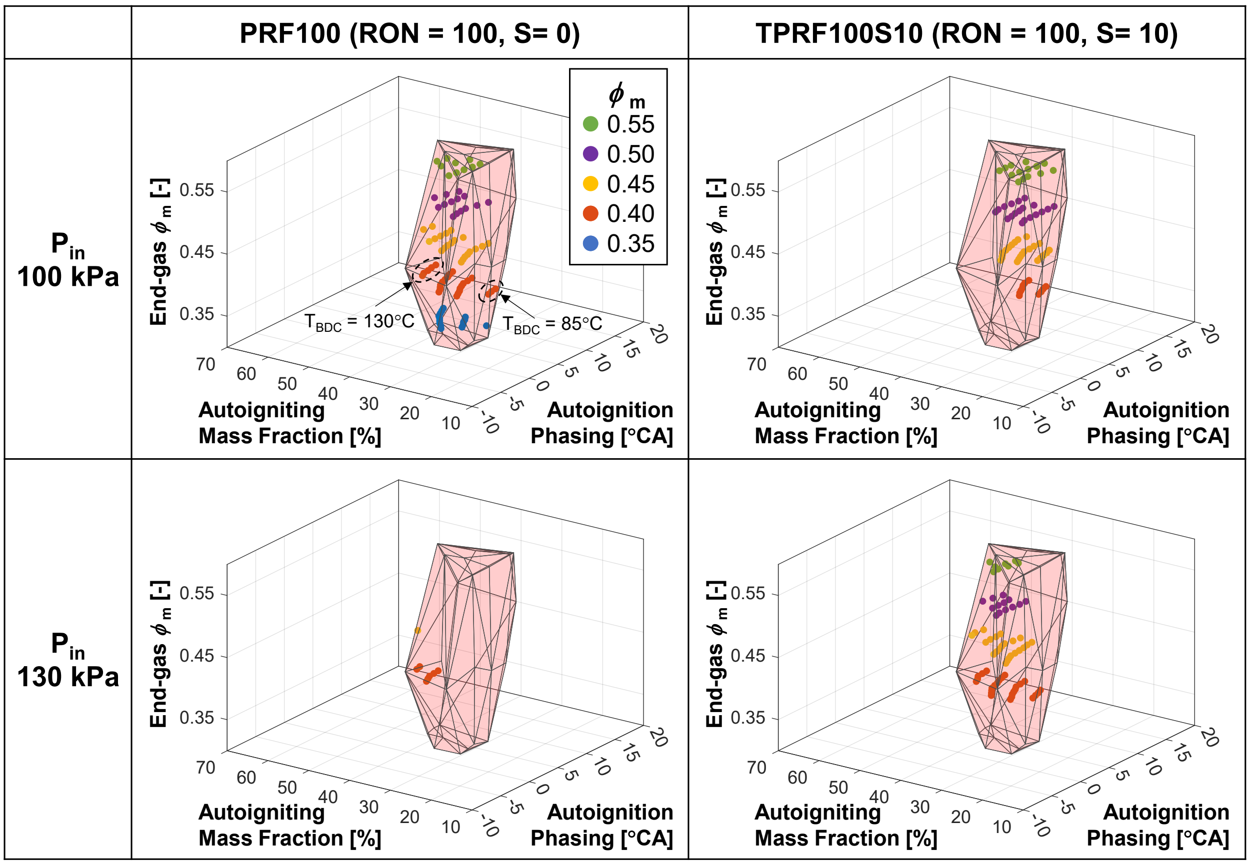

Figure 13. Simulated autoignition phasing and mass fraction as a function of ϕ_m, engine speed, and CA50 for PRF100 and TPRF100S10 at CR=12, 1400 rpm, P_{in}= 100 and 130 kPa. The operable operating regime is indicated by the pink-colored manifold (identical to that shown in Fig. 9(a)) and operable conditions are shown by solid markers.

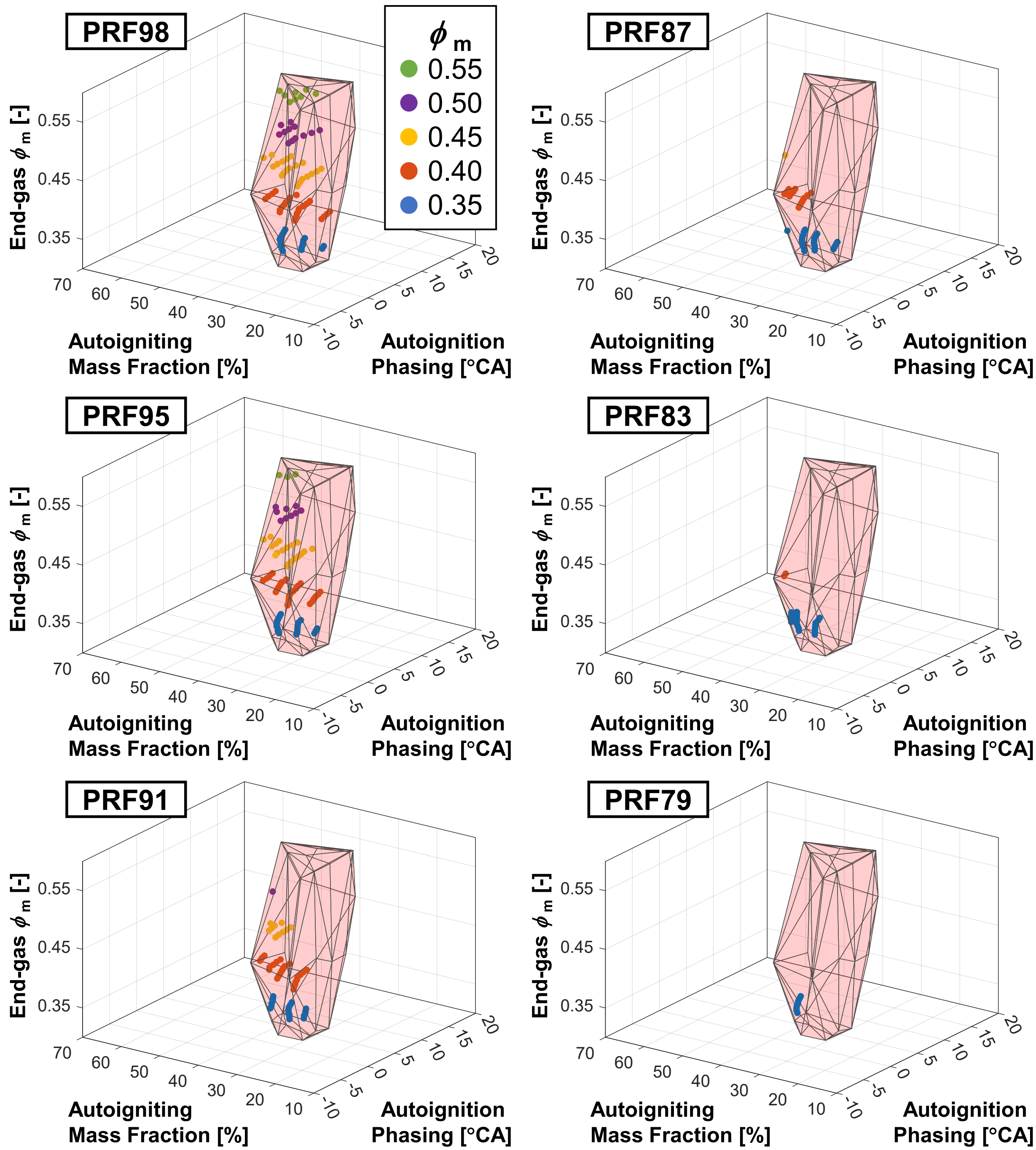

Figure 14: Simulated autoignition phasing and mass fraction as a function of ϕ_m, and CA50 over a range of PRF fuels for CR = 12, 1400 rpm, P_{in} = 100 kPa. Operable conditions are shown by solid markers inside the pink-colored manifold.

The operability ranges (high- and low-load limits) of PRFs and TPRFs at each CR and engine speed are presented in Fig. 15. For brevity, only the data for CR = 12 and 14 are shown. The figure shows the net effects of the changes in operability which were demonstrated for selected fuels in Figs. 13 and 14. Trendlines from linear regressions are added to better show the trend in minimum and maximum $IMEP_g$. The individual data points sometimes display no effect of RON, followed by larger steps. This happens because of the limited resolution of P_{in} and ϕ_m spanned for the GT-Power simulations.

The operating ranges for CR = 12 which are shown in Fig. 15 (a) demonstrate significant differences in the range of predicted operation at 1000 rpm, ranging from minimal or no operability for many fuels (too reactive) to nearly full operability at 1000 rpm for the most knock-resistant fuels (high-RON, high-S). In the case of the more reactive fuels at this engine speed, typically only the lowest T_{BDC} and P_{in} condition (85°C and 85 kPa) is operable, and the load range is achieved through varying ST and ϕ_m. Conversely, high-RON, high-S fuels are able to operate at high P_{in} and ϕ_m combinations, resulting in a much higher maximum $IMEP_g$. Also, high-RON, high-S fuels exhibit only a slight increase in minimum $IMEP_g$, rendering an overall wider load range. The 1400 rpm condition shown in Fig. 15 (c) exhibits trends similar to the 1000 rpm conditions. However, by nature of the higher engine speed, which affords less time for autoignition reactions to occur, higher reactivity fuels do exhibit wider operability than at 1000 rpm.

When CR is raised from 12 to 14 at engine speeds 1000 – 1400 rpm, Figs. 15 (a) through (d) show that the operable range significantly shrinks for all fuels. This is somewhat expected because the higher CR leads to higher compressed-gas temperatures and pressures near TDC that promote autoignition reactivity. However, high-RON, high-S fuels retain a sizeable operable range. It can be noted that for a given high RON at CR = 14, increased S strongly increases the upper load limit and even expands the lower load limit. This demonstrates that high-S fuels are favored for MMC at a higher CR as well.

As the engine speed is increased to 2000 rpm, the trends change significantly relative to the lower-speed cases, especially for the higher CR. Figure 15 (f) shows that even the low-RON zero-S fuels achieve a moderate load range. The model predicts that S=10 fuels may operate at P_{in} = 130 kPa with moderately high ϕ_m. This is likely due to the shorter timescales for autoignition, which will particularly inhibit low-temperature oxygen-addition reactions which are characteristically slow [33]. In addition, the volume of the combustion chamber expands faster, effectively shortening the time available for high-temperature reactions that lead to autoignition of the mixture. Another observation made for 2000 rpm, CR=12 (Fig. 15(e)) is that S = 10 fuels do not show an increase in maximum $IMEP_g$ with RON. This is because for TPRF100S10, TPRF98S10, and TPRF95S10, the model predicts that all three fuels achieve maximum $IMEP_g$ at P_{in} = 130 kPa, T_{BDC} = 85°C, and ϕ_m = 0.55 but at different ST. CA50 at maximum $IMEP_g$ for TPRF95S10 is predicted to be 6°CA whereas it is 1°CA for TPRF100S10. Because the typical CA50 that yields the maximum $IMEP_g$ for lean operation ($\phi_m \approx 0.5$) is typically around 5°CA, slightly higher $IMEP_g$ for TPRF95S10 is observed. If ϕ_m greater than 0.55 was spanned, or P_{in} was allowed to be greater than 130 kPa, the trend for S = 10 fuels is expected to resemble those observed at lower engine speeds.

The predicted operability ranges provide a number of useful insights into the interactions between the fuels, the combustion mode and the operating strategy. At a fixed RON level, the fuels with higher S exhibit a wider operating range. Also, for the examined conditions, namely engine speeds between 1000 – 2000 rpm, CR = 12 and 14, lower RON fuels were not observed to provide an operability benefit over higher RON fuels at low loads. Considering the CRs of modern engines [31, 32, 34], as well as modern vehicle calibration and drive-cycle conditions [31], the results suggest that there is not a strong synergy between low-RON fuels and this combustion system in a multimode implementation. Conversely, a strong synergy is expected between high-RON and high-S fuels for both MMC at applicable conditions as well as for boosted stoichiometric SI operation, which extends to beyond-RON conditions and therefore also benefits from fuels with higher RON and higher S [12, 35-38].

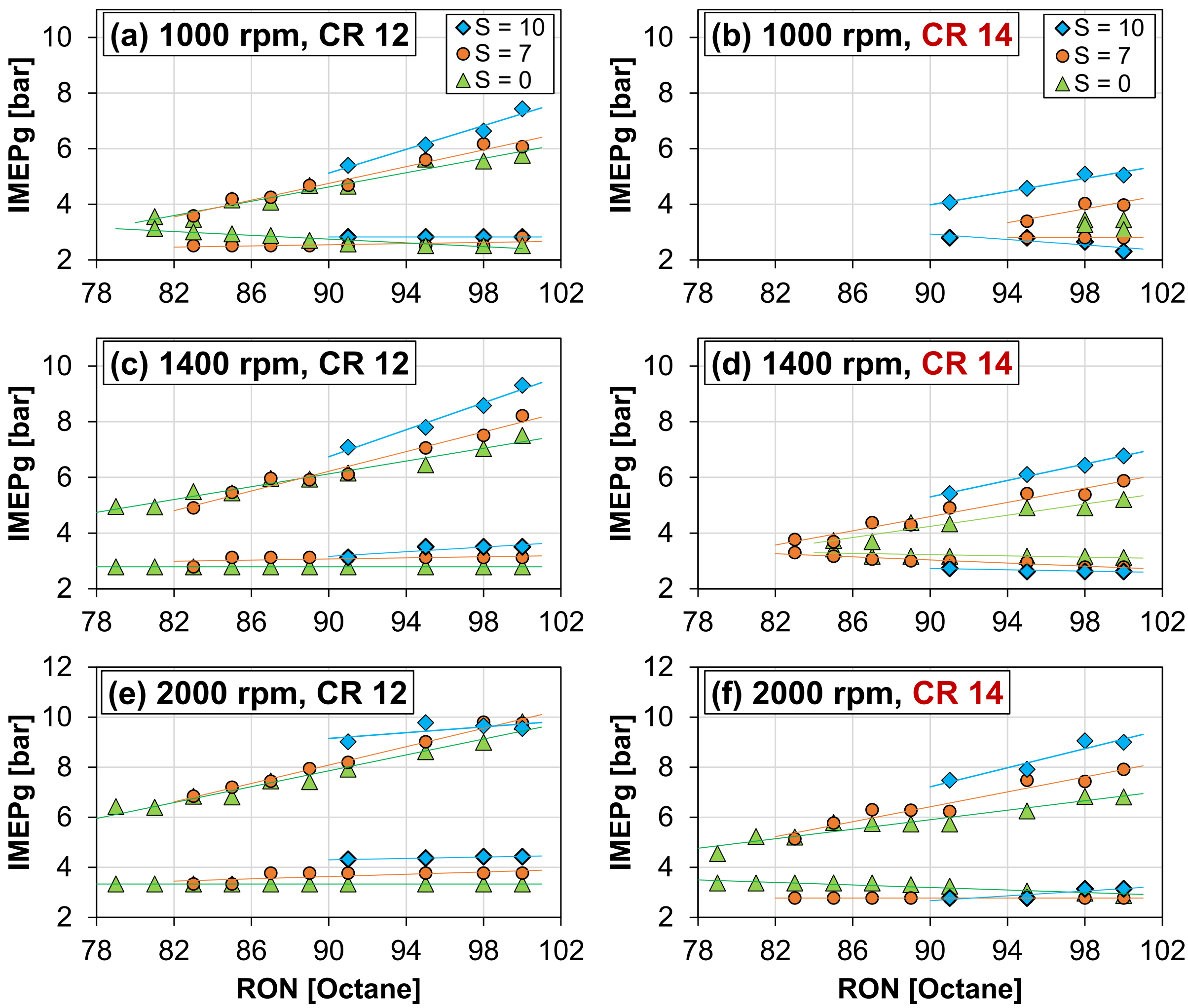

Figure 15: Simulated maximum and minimum $IMEP_g$ of PRFs and TPRFs as a function of RON for (a) 1000 rpm, CR = 12, (b) 1000 rpm, CR = 14, (c) 1400 rpm, CR = 12, (d) 1400 rpm, CR = 14, (e) 2000 rpm, CR = 12, and (f) 2000 rpm, CR = 14.

As demonstrated in Fig. 15, higher RON and S fuels are expected to achieve broader operable range compared to lower RON and S fuels. To put this into a context with potential impact to fuel economy, the model results were utilized to construct brake efficiency maps as mentioned in the methodology section. The MMC brake efficiency map was overlaid onto that of a conventional naturally aspirated SI engine using the information from EPA's benchmarking [31]. In addition, to provide insights on how a difference in the load coverage for given fuels could influence fuel economy, a contour is added which represents an approximate extent of conditions contributing significantly to the combined City and Highway Fuel Economy Tests [31]. An example of the brake efficiency maps for MMC for PRF89 and TPRF100S10 are shown in Fig. 16. The data correspond to CR = 13 given that the engine that EPA benchmarked had CR = 13.

Figure 16(a) shows that MMC can offer considerable efficiency benefits, ranging up to ~10%. However, compared to TPRF100S10, MMC based on PRF89 covers less than half of operating conditions relevant for drive cycle tests. In addition, PRF89 can only achieve lower loads where the fuel flowrate is lower than for the higher loads, which would offer reduced gain in fuel economy. Figure 16(b) shows that TPRF100S10 offers slightly reduced efficiency gain for BMEP < 4 bar compared to PRF89. It was found that due to lower reactivity of TPRF100S10, the lower load limits are achieved by operating the engine at very early CA50 (i.e. -10°CA) which is unfavorable from an efficiency standpoint. Nevertheless, TPRF100S10 can enable up to 10% improvement in brake efficiency for BMEP > 5 bar. Moreover, MMC with TPRF100S10 covers much higher loads where the fuel flowrates are greater. Hence, TPRF100S10 has a greater potential to maximize fuel economy gain enabled by MMC.

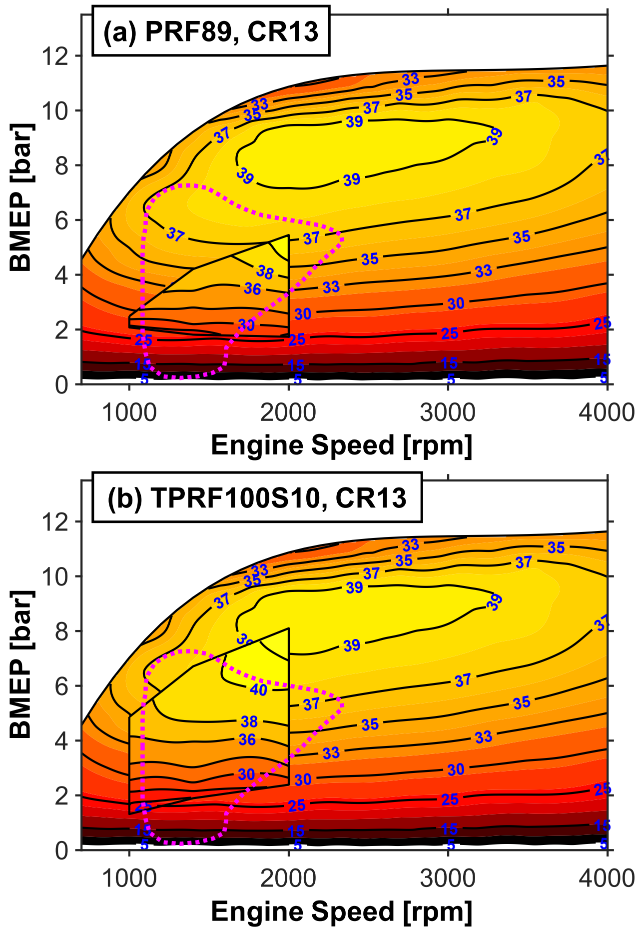

Figure 16: Simulated operating range and brake efficiencies of (a) PRF89 and (b) TPRF100S10 at CR = 13. MMC includes operations using P_{in} = 85 – 130 kPa. Also indicted by the dashed red line is the extent of combined city and highway regulatory cycles obtained from benchmarking a mid-sized sedan with best-in-class fuel economy [31].

To further increase the load coverage of MMC using TPRF100S10 for BMEP < 2 bar, MMC can be coupled with other combustion mode such as stratified-charge combustion system, which can cover down to near zero BMEP. Another viable pathway would be to combine the MMC system with an electric-hybrid powertrain so that lower load coverage of MMC could be replaced with operation by an electric motor. Lastly, cylinder deactivation can be considered. An example is shown in Fig. 17 to demonstrate the impact of deactivating two of four cylinders on lower load coverage. The example also shows the improved efficiency at BMEP < 4 bar. This is attributed to avoiding operation with overly advanced CA50 that deteriorates the efficiency gain from MMC. Considering the good coverage of the drive cycles, as well as the higher projected efficiency of the MMC system in this range (by nature of improved specific heat ratio and lower heat losses – typically on the order of 5 – 20% improvement), such a combustion system would likely significantly improve the rated fuel economy, although no formal assessment is made here, as this is beyond the scope of the study.

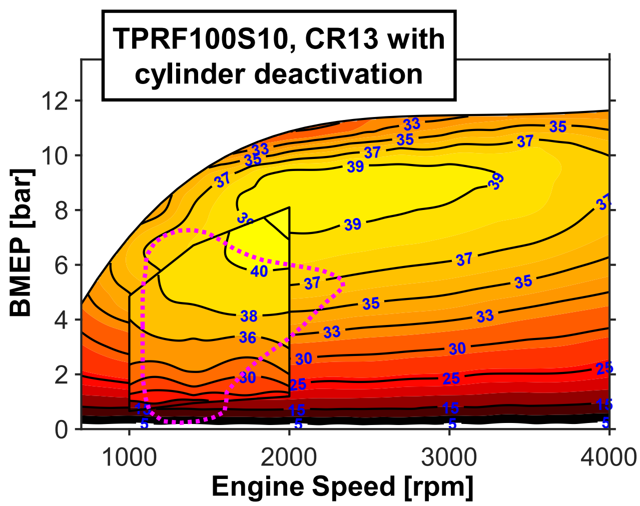

Figure 17: Simulated operating range and brake efficiencies of the TPRF100S10 fuel for CR = 13 with MMC operation that includes boost and cylinder deactivation (two of four cylinders).

Conclusions

This study combined a 1-D two-zone engine model with a 0-D chemical-kinetic autoignition model to predict fuel effects on the achievable load range of an engine operating with Mixed-Mode Combustion (MMC), which combines deflagration and autoignition. After the 1-

D / 0-D model framework was validated using experimental data, the model was used to determine the minimum and maximum $IMEP_g$ for varying fuel octane ratings, expressed in terms of RON and S. The MMC combustion system was operated at conditions that are relevant to modern light-duty vehicles when implemented in a multimode system which combines MMC and conventional stoichiometric spark-ignition operation. The modeling results indicated a strong synergy between the octane appetite of a boosted stoichiometric spark-ignition engine and that of the MMC combustion system. Both combustion modes benefit from fuels with high-RON and high-S, which enable broad operability over the speed-load space. This result nullified the hypothesis that a more reactive fuel would provide operational benefits by allowing MMC operation with significantly lower loads. Utilizing the model output, the load-speed ranges which were predicted were compared with those necessary for operation in Federal fuel economy tests for a mid-sized sedan, and it was found that although MMC can provide high brake efficiencies at particular operating points, load coverage over the drive-cycle may be challenging, and require additional technologies in order to be effective, such as cylinder deactivation or an additional combustion mode optimized for low loads.

The results of the modeling and validation experiments indicated areas in which further research is warranted. In particular, the MMC experiments at 2000 rpm indicate that phenomena such as cycle-to-cycle variability and the relationship between autoignition and acoustic knock determine operability, and these controlling behavior must be better understood. This stands in contrast with MMC operation at lower engine speeds where the intersection of a fuel's autoignition behavior with the boundary conditions and timescales of the piston-driven compression and expansion is the chief determinant of operability.

Acknowledgment

The authors would like to thank Alberto Garcia, Keith Penney, Nathan Harry, Aaron Czeszynski and Tim Gilbertson for their dedicated support of the Alternative Fuels DISI Engine Laboratory. Dario Lopez-Pintor and Seokwon Cho provided valuable feedback on the manuscript.

The authors express gratitude towards William Pitz, Scott Wagnon, Matthew McNenly, Simon Lapointe and Chiara Saggese of Lawrence-Livermore National Laboratory for assistance with the detailed chemical-kinetics model, fuel-surrogate formulation and supporting calculations.

Financial support for this study was provided Co-Optimization of Fuels & Engines (Co-Optima) project. Support for establishing the engine lab used in this study was provided by the Vehicle Technologies Office at U.S. Department of Energy (DOE), Office of Energy Efficiency and Renewable Energy (EERE). Sandia National Laboratories is a multi-mission laboratory managed and operated by National Technology and Engineering Solutions of Sandia, LLC., a wholly owned subsidiary of Honeywell International, Inc., for the U.S. Department of Energy's National Nuclear Security Administration under contract DE-NA0003525.

This paper describes objective technical results and analysis. Any subjective views or opinions that might be expressed in the paper do not necessarily represent the views of the U.S. Department of Energy or the United States Government.

References

[1] Doornbos, G., Hemdal, S., Dahl, D., and Denbratt, I., "Transient Responses of Various Ammonia Formation Catalyst Configurations for Passive SCR in Lean-Burning Gasoline

Engines under Various Real Engine Conditions.," SAE Technical Paper 2016-01-0935, 2016, doi:10.4271/2016-01-0935.

[2] Dempsey, A.B., Curran, S.J., and Wagner, R.M., “A perspective on the range of gasoline compression ignition combustion strategies for high engine efficiency and low NOx and soot emissions: Effects of in-cylinder fuel stratification,” International Journal of Engine Research 17(8):897-917, 2016, doi:10.1177/1468087415621805.

[3] Splitter, D.A. and Reitz, R.D., “Fuel reactivity effects on the efficiency and operational window of dual-fuel compression ignition engines,” Fuel 118:163-175, 2014, doi:10.1016/j.fuel.2013.10.045.

[4] Baškovič, U.Ž., Oprešnik, S.R., Seljak, T. and Katrašnik, T., “RCCI combustion with renewable fuel mix–Tailoring operating parameters to minimize exhaust emissions,” Fuel 311: 122590, 2022, doi:10.1016/j.fuel.2021.122590.

[5] Sjöberg, M., Zeng, W., and Reuss, D., "Role of Engine Speed and In-Cylinder Flow Field for Stratified and Well-Mixed DISI Engine Combustion Using E70," SAE International Journal of Engines 7(2):642-655, 2014, doi:10.4271/2014-01-1241.

[6] Zeng, W., Sjöberg, M., Reuss, D.L., and Hu, Z., “The role of spray-enhanced swirl flow for combustion stabilization in a stratified-charge DISI engine,” Combustion and Flame 168:166-185, 2016, doi:10.1016/j.combustflame.2016.03.015.

[7] Iida, N., Yokomori, T., Tsue, M., Kitagawa, T., Kosaka, H., Miyoshi, A. and Moriyoshi, Y., “Research and Development on Super Lean Burn Combustion for High Efficiency SI Engines”, Journal of the Combustion Society of Japan 61(197):178-192, 2019, doi: 10.20619/jcombsj.61.197_178.

[8] Hu, Z., Zhang, J., Sjöberg, M. and Zeng, W., “The use of partial fuel stratification to enable stable ultra-lean deflagration-based Spark-Ignition engine operation with controlled end-gas autoignition of gasoline and E85,” International Journal of Engine Research 21(9), pp.1678-1695, 2020, doi: 10.1177/1468087419889702.

[9] Singh, E., Vuillermier, D., Kim, N., and Sjöberg, M., “Influence of Gasoline Fuel Formulation on Lean Autoignition in a Mixed-Mode-Combustion (Deflagration/Autoignition) Engine,” Combustion and Flame 242:112163, 2022, doi:10.1016/j.combustflame.2022.112163

[10] Ayala, F. and Heywood, J., "Lean SI Engines: The role of combustion variability in defining lean limits," SAE Technical Paper 2007-24-0030, 2007, doi:10.4271/2007-24-0030.

[11] Nakai, E., Goto, T., Ezumi, K., Tsumura, Y., Endou, K., Kanda, Y., Urushihara, T., Sueoka, M., and Hitomi, M., “Mazda Skyactiv-X 2.0 L gasoline engine,” 28th Aachen colloquium automobile and engine technology, 2019.

[12] Szybist, J.P., Busch, S., McCormick, R.L., Pihl, J.A., Splitter, D.A., Ratcliff, M.A., Kolodziej, C.P., Storey, J.M.E., Moses-DeBusk, M., Vuilleumier, D. et al., “What fuel properties enable higher thermal efficiency in spark-ignited engines?” Progress in Energy and Combustion Science 82:100876, 2021, doi:10.1016/j.pecs.2020.100876.

[13] Xu, C., Som, S. and Sjöberg, M., "Large eddy simulation of lean mixed-mode combustion assisted by partial fuel stratification in a spark-ignition engine," Journal of Energy Resources Technology 143(7): 072304, 2021, doi:10.1115/1.4050588.

[14] Xu, C., Pal, P., Ren, X., Sjöberg, M., Van Dam, N., Wu, Y., Lu, T., McNenly, M. and Som, S., "Numerical investigation of fuel property effects on mixed-mode combustion in a spark-ignition engine." Journal of Energy Resources Technology 143(4):042306, 2021, doi:10.1115/1.4048242.

[15] Bozza, F., Siano, D., and Torella, E., "Cycle-by-Cycle Analysis, Knock Modeling and Spark-Advance Setting of a “Downsized” Spark-Ignition Turbocharged Engine," SAE International Journal of Engines 2(2):381-389, 2010, doi:10.4271/2009-24-0020.

[16] Khan, Ahmed Faraz, Philip John Roberts, and Alexey A. Burluka. "Modelling of self-ignition in Spark-Ignition engine using reduced chemical kinetics for gasoline surrogates," Fluids 4(3):157, 2019, doi:10.3390/fluids4030157.

[17] Shah, A., Cheng, S., Longman, D.E., Goldsborough, S.S. and Rockstroh, T., “An experimental study of uncertainty considerations associated with predicting auto-ignition timing using the Livengood-Wu integral method,” Fuel 286:119025, 2021, doi:10.1016/j.fuel.2020.119025.

[18] Zeng, W., Sjöberg, M. and Reuss, D.L., “PIV examination of spray-enhanced swirl flow for combustion stabilization in a spray-guided stratified-charge direct-injection spark-ignition engine,” International Journal of Engine Research, 16(3):306-322, 2015, doi:10.1177/1468087414564605.

[19] Tornatore, C. and Sjöberg, M., “Optical Investigation of a Partial Fuel Stratification Strategy to Stabilize Overall Lean Operation of a DISI Engine Fueled with Gasoline and E30,” Energies, 14(2):396, 2021, doi:10.3390/en14020396.

[20] Heywood, J.B., Internal Combustion Engine Fundamentals, McGraw-Hill, New York, 1988.

[21] GT-Power, Gamma Technologies, 2018.

[22] Wiebe, I. I. Semi-empirical expression for combustion rate in engines. In Proceedings of Conference on Piston engines, USSR, 1956, pp. 185–191. (Academy of Sciences, Moscow)

[23] Reuss, D.L., Kim, N. and Sjöberg, M., "The influence of intake flow and coolant temperature on gasoline spray morphology during early-injection DISI engine operation," International Journal of Engine Research (2022): 14680874221104301.

[24] ANSYS CHEMKIN-PRO 18.1, ANSYS: San Diego, 2017.

[25] Westbrook, C.K., Sjöberg, M. and Cernansky, N.P., "A New Chemical Kinetic Method of Determining RON and MON Values for Single Component and Multicomponent Mixtures of Engine Fuels," Combustion and Flame, 195:50-62, 2018, doi:10.1016/j.combustflame.2018.03.038

[26] Vuilleumier, D., Kim, N., Sjöberg, M., Yokoo, N., Tomoda, T. and Nakata, K., "Effects of EGR Constituents and Fuel Composition on DISI Engine Knock: An Experimental and Modeling Study," SAE Technical Paper 2018-01-1677, 2018, doi:10.4271/2018-01-1677.

[27] Kim, N., Vuilleumier, D., Sjöberg, M., Yokoo, N., Tomoda, T. and Nakata, K., "Using Chemical Kinetics to Understand Effects of Fuel Type and Compression Ratio on Knock-Mitigation Effectiveness of Various EGR Constituents," SAE Int. J. Adv. & Curr. Prac. in Mobility 1(4):1560-1580, 2019, doi:10.4271/2019-01-1140.

[28] Mehl, M., Pitz, W.J., Westbrook, C.K, and Curran, H.J., "Kinetic modeling of gasoline surrogate components and mixtures under engine conditions." Proceedings of the Combustion Institute 33, no. 1 (2011): 193-200.

[29] Lopez Pintor, D., Dec, J., and Gentz, G., "Φ-Sensitivity for LTGC Engines: Understanding the Fundamentals and Tailoring Fuel Blends to Maximize This Property," SAE Technical Paper 2019-01-0961, 2019, doi:10.4271/2019-01-0961.

[30] Sjöberg, M., Kim, N., Matsubara, N., Yokoo, N. and Nakata, K., "Influence of Nitric Oxide and Other Factors on Acoustic Knock Onset for Lean DISI Engine Operation," The International Conference on Modeling and Diagnostics for Advanced Engine Systems 2022(10):0094, 2022.

[31] Kargul, J., Stuhldreher, M., Barba, D., Schenk, C. Bohac, S., McDonald, J. and Dekraker, P., "Benchmarking a 2018 Toyota Camry 2.5-Liter Atkinson Cycle Engine with Cooled-EGR," SAE Int. J. Adv. & Curr. Prac. in Mobility 1(2):601-638, 2019, doi:10.4271/2019-01-0249.

[32] Stuhldreher, M., "Fuel Efficiency Mapping of a 2014 6-Cylinder GM EcoTec 4.3 L Engine with Cylinder Deactivation," SAE Technical Paper 2016-01-0662, 2016, doi:10.4271/2016-01-0662.

[33] Vuilleumier, D., Kozarac, D., Mehl, M., Saxena, S., Pitz, W.J., Dibble, R.W., Chen, JY. and Sarathy, S.M., "Intermediate temperature heat release in an HCCI engine fueled by ethanol/n-heptane mixtures: An experimental and modeling study," Combustion and Flame, 161(3):680-695, 2014, doi:10.1016/j.combustflame.2013.10.008.

[34] Ellies, B., Schenk, C., and Dekraker, P., "Benchmarking and Hardware-in-the-Loop Operation of a 2014 MAZDA SkyActiv 2.0 L 13:1 Compression Ratio Engine," SAE Technical Paper 2016-01-1007, 2016, doi:10.4271/2016-01-1007.

[35] Vuilleumier, D. and Sjöberg, M., "The Use of Transient Operation to Evaluate Fuel Effects on Knock Limits Well beyond RON Conditions in Spark-Ignition Engines," SAE Technical Paper 2017-01-2234, 2017, doi:10.4271/2017-01-2234.

[36] Mittal, V. and Heywood, J., "The Relevance of Fuel RON and MON to Knock Onset in Modern SI Engines," SAE Technical Paper 2008-01-2414, 2008, doi:10.4271/2008-01-2414.

[37] Farrell, J.T., Zigler, B.T., Ratcliff, M.A., Miles, P. Kolodziej, C., Sjöberg, M., Sluder, S., Szybist, J., Wagner, S., Splitter, D. et al., "Co-optimization of fuels & engines: Efficiency merit

function for spark-ignition engines; revisions and improvements based on fy16-17 research," Report No. NREL/TP-5400-67584; DOE/GO-102018-5041, Golden, CO: National Renewable Energy Laboratory, 2018.

[38] Szybist, J.P. and Splitter, D.A., "Understanding chemistry-specific fuel differences at a constant RON in a boosted SI engine," Fuel, 217:370-381, 2018, doi:10.1016/j.fuel.2017.12.100.

TOC Graphic